Solid Earth Discuss., 6, 1–36, 2015
www.solid-earth-discuss.net/6/1/2015/
doi:10.5194/sed-6-1-2015

Solid Earth Discussions
Open Access

POLENET/LAPNET teleseismic P-wave traveltime tomography model of the upper mantle beneath northern Fennoscandia

H. Silvennoinen[1,2], **E. Kozlovskaya**[2,1], **and E. Kissling**[3]

[1]Sodankylä Geophysical Observatory, University of Oulu, P.O. Box 3000, 90014 Oulu, Finland
[2]Oulu Mining School, University of Oulu, P.O. Box 3000, 90014 Oulu, Finland
[3]Institute of Geophysics, ETH Zürich, Sonneggstrasse 5, 8092 Zürich, Switzerland

Received: 22 August 2015 – Accepted: 25 August 2015 – Published:

Correspondence to: H. Silvennoinen (hanna.silvennoinen@oulu.fi)

Published by Copernicus Publications on behalf of the European Geosciences Union.

Abstract

The POLENET/LAPNET broadband seismic array was deployed in northern Fennoscandia (Finland, Sweden, Norway, and Russia) during the third International Polar Year 2007–2009. The array consisted of roughly 60 seismic stations. In our study we estimate the 3-D architecture of the upper mantle beneath the northern Fennoscandian shield using high-resolution teleseismic P-wave tomography. For this purpose 111 clearly recorded teleseismic events were selected and the data from the stations hand-picked and analysed. Our study reveals a highly heterogeneous lithospheric mantle beneath the northern Fennoscandian shield though without any large high P-wave velocity area that may indicate presence of thick depleted lithospheric "keel". The most significant feature seen in the velocity model is a large elongated negative velocity anomaly (up to −3.5 %) in depth range 100–150 km in the central part of our study area that can be followed down to a depth of 200 km in some local areas. This low-velocity area separates three high-velocity regions corresponding to the cratons and it extends to greater depth below the Karelian craton.

1 Introduction

Recently, dense two-dimensional (2-D) arrays of broadband seismic instruments have proved to be a most effective mean to study the 3-D structure of the lithosphere and the lithosphere–asthenosphere boundary (LAB) (Trampert and Van der Hilst, 2005). One of such arrays was the POLENET/LAPNET broadband seismic array (http://www.oulu.fi/sgo-oty/lapnet) deployed in northern Fennoscandia (Finland, Sweden, Norway, and Russia) during the third International Polar Year 2007–2009. The project was a part of POLENET (POLar Earth observing NETwork, http://www.polenet.org) consortium. The array consisted of 37 temporary and 21 permanent seismic stations (Fig. 1). All the stations, except of 2 temporary stations, were the broadband one

SED
6, 1–36, 2015

The array registered waveforms from teleseismic, regional and local events during May 2007–September 2009. The average distance between stations was 70 km.

One of the main targets of POLENET/LAPNET was to obtain a 3-D seismic model of the upper mantle in northern Fennoscandian Shield, in particular, beneath its Archaean domain (Fig. 1), as the area has not been studied previously by dense broadband seismic arrays. Since 1980–1990, after discovery of two large diamond deposits in its north-eastern margin (close to the city Archangelsk in Russia), the area is considered to be prospective for diamondiferous kimberlitic rocks. This supposition is based on three empirically established factors necessary for diamond preservation: Archean bedrock, a low geothermal gradient and a thick lithosphere (Clifford, 1966).

As shown by Snyder et al. (2004), recordings of teleseismic events can be used to explore the mantle lithosphere to depths of several hundreds kilometres, and through geological interpretations, to assess its potential as a diamond reservoir. Generally, such modelling of the upper mantle needs to include P- and S-wave velocity models estimated by teleseismic body wave tomography, position of major boundaries in the crust and upper mantle estimated by controlled source seismic (CSS) and/or receiver function techniques and strength and orientation of seismic anisotropy that can be assessed by shear-wave splitting, receiver function analysis, or ambient noise tomography. Such a combined seismic model makes it possible to evaluate the thickness and composition of the mantle lithosphere beneath the study area. It may further be used for 3-D mapping of lithospheric architecture and structures responsible for formation, accumulation and preservation of economically significant mineral deposits (Laznicka, 2014; Mole et al., 2014).

In our study we explore the 3-D P-wave architecture of the upper mantle beneath the northern Fennoscandian Shield using high-resolution teleseismic tomography. This technique was used by Sandoval et al. (2004), who obtained a 3-D P-wave velocity model of the upper mantle beneath the southeastern Fennoscandian shield documenting a deep lithospheric "keel" structure beneath that region. Similar technique was used also by Shomali et al. (2006) and Janutyte et al. (2014), in order to study the upper

SED
6, 1–36, 2015

mantle structure in the transition zone between Precambrian Fennoscandian Shield and Palaeozoic lithosphere of ~~the~~ Western Europe. Eken et al. (2007) used teleseismic tomography with data of the Swedish National Seismic Network, in order to estimate the upper mantle structure beneath Sweden. The data of the POLENET/LAPNET experiment were used by Plomerová et al. (2011) and Vinnik et al. (2014), who estimated seismic anisotropy in the upper mantle beneath the POLENET/LAPNET study area. Vinnik et al. (2015) report on variations of S- and P-wave velocities and Vp/Vs ratio beneath the POLENET/LAPNET array using joint inversion of P- and S- receiver functions. Our study thus complements the previous studies of the upper mantle in the Fennoscandia by body-wave tomography technique. It is also a valuable contribution to the combined seismic model of the upper mantle beneath the northern Fennoscandian shield.

2 Tectonic setting

Our study area is located in the Fennoscandian Shield in the northern part of the East European Craton. The area consists of the Archaean Karelian Craton in the eastern part of the study area, subdivided to Karelian and Kola Provinces and Belomorian Mobile Belt in between, the Svecofennian Norbotten Craton in the western part and the Caledonides in north-western corner (Fig. 1b).

The Karelian Craton started rifting in Palaeoproterozoic some 2.5–2.1 Ga ago. Rifting began in northeast and led to separation of cratonic components by oceans around 2.1 Ga (Daly et al., 2006). The rifting event was follows by two orogenies: the Lapland-Kola orogeny (1.94–1.86 Ga, Daly et al., 2006) and the northern part of Svecofennian orogeny (1.92–1.89 Ga, Lahtinen et al., 2008) (Fig. 1a).

The Lapland-Kola orogeny was preceded by subduction of the new oceanic crust and by island arc accretion at 1.95–1.91 Ga. The orogeny was a transpressional continent-continent collision between Kola Province and Karelian Province and produced only a minimal amount of juvenile material (Lahtinen et al., 2008). Although in general Sve-

SED
6, 1–36, 2015

cofennian orogeny formed a large unit of new Palaeoproterozoic crust. Similarly to the Lapland-Kola orogeny, its northern part mainly comprises of reworked Archean crust. The orogeny began from north, where the Karelian Craton and Norbotten craton collided at ca. 1.92 Ga (Lahtinen et al., 2008, 2015).

After these two orogenies there has been no major tectonic events in our study area, but there are still some smaller volume magmatism with ages from Palaeoproterozoic to Devonian (Downes et al., 2005). These rocks are often from relatively deep source and, though quite diverse in rock types, are some of the most important carriers of mantle xenoliths (Woodard, 2010).

3 Dataset

The main data set used in this study is the data of POLENET/LAPNET array that recorded during May 2007–September 2009. For this study we selected 96 teleseismic events that were located at ~~the~~ epicentral distances between 30 and 90° from our station array and were clearly recorded by most of the stations. Most of the selected events have magnitudes larger than 6.0, but events with magnitudes larger than 5.5 were also considered in order to improve the azimuthal coverage. In this way we obtained a good coverage over all back-azimuths (see Fig. 2); the largest azimuthal gap in events recorded by POLENET/LAPNET array is smaller than 15 degrees. The first arrivals of P-waves were picked manually using Seismic-Handler software (http://www.seismic-handler.org/). We used the WWSSN short period simulation filter for easier comparison between waveforms recorded by different types of sensors. The traveltime residuals were calculated using ~~IASP91~~ reference model (Kennett and Engdahl, 1991). While picking the arrivals, the uncertainty of each arrival time was also estimated. The picked arrival times were then divided into 3 quality classes based on individual uncertainty estimates. Table 1 shows the error estimates for each class and the number of arrival times attributed to different classes. Example wave forms with arrival time picks of different quality are shown in Fig. 3.

SED
6, 1–36, 2015

"Raw" residuals calculated as differences between observed and theoretical arrival times using ~~IASP91~~ velocity model and ISC catalogue hypocentre parameters exhibit large amplitudes while showing only small azimuthal variations between stations (see Fig. 4~~a~~). This is the combined effect of deep mantle velocity variations located outside our study volume and of near-source structure or teleseismic hypocentre parameter uncertainties. To separate those effects from our observations, the average traveltime residual over all stations was calculated for each event and ~~reduced~~ from all corresponding residuals. The resulting residuals contain the effects of the velocity variations within our study volume with reference to ~~IASP91~~ model. Fig. 4~~b~~ shows the azimuthal distributions of residuals for ~~eight~~ selected stations representing different regions within our study area.

In addition to the new dataset from the POLENET/LAPNET array we included to our study previous data from the northern part of the SVEKALAPKO array (Hjelt et al., 2006) located south of POLENET/LAPNET array but still within our study area. This additional data included 15 events recorded at 31 stations yielding 360 P-wave residual times (Plomerová et al., 2006). The quality classes of the SVEKALAPKO data are shown in Table 1. All seismic stations included in this study are shown in Fig. 1b) and the event distribution is shown in Fig. 2.

4 The inversion method

In seismic tomography, the basic system of equations relating velocity perturbations inside the study volume to traveltime residuals is

$$\boldsymbol{d} = \mathbf{G}\boldsymbol{m}, \tag{1}$$

where $\boldsymbol{d}$ is a data vector composed of traveltime residuals, $\boldsymbol{m}$ is a model parameter vector composed of velocity perturbations in each cell of the velocity model and $\mathbf{G}$ is a matrix of partial derivatives defining the coupling between data and model parameters (e.g., Kissling, 1988). The method searches the velocity perturbations inside the

SED
6, 1–36, 2015

defined 3-D model in order to explain the observed traveltime residuals. In teleseismic tomography, velocities outside and initial velocities inside the study volumes are approximated using a reference model. The reference model used in this study is IASP91 (Kennett and Engdahl, 1991).

For the inversion of the P-wave residual data, we used TELINV, a non-linear tomographic inversion program, originally developed by Evans and Achauer (1993), who applied the AHC tomographic method by Aki et al. (1977) to lithosphere investigations at regional scale, and later modified by several authors (e.g., Weiland et al., 1995; Arlitt et al., 1999; Lippitsch et al., 2003; Sandoval et al., 2004) to include 3-D ray tracing and iterative non-linear inversions.

The initial 3-D model is defined as an orthogonal grid of nodes approximating the study volume, where the velocity is defined at the node points. The traveltime calculation is based on the 3-D Simplex ray-tracing technique (Steck and Prothero, 1991). Inversion problem is formulated as a weighted damped least square problem and solved using Singular Value Decomposition (SVD) technique. The overall non-linear inversion scheme iteratively inverts the traveltime residuals for velocity changes relative to the 3-D velocity model of the previous iteration, beginning with the initial reference 3-D model. Each iteration involves a complete one-step inversion, including both ray tracing (forward problem) and inversion for an update of the velocity distribution in the model.

The basic inversion equation for the TELINV code can be written as

$$\boldsymbol{m}_{\text{est}} = (\mathbf{G}^{\mathrm{T}}\mathbf{W}_{\mathrm{D}}\mathbf{G} + \varepsilon^2\mathbf{W}_{\mathrm{M}})^{-1}\mathbf{G}^{\mathrm{T}}\mathbf{W}_{\mathrm{D}}\boldsymbol{d}, \quad (2)$$

where $\boldsymbol{m}_{\text{est}}$ are estimated model parameters, $\mathbf{W}_{\mathrm{D}}$ is the weighting matrix of the data, ε^2 is a damping factor, and $\mathbf{W}_{\mathrm{M}}$ is the smoothing matrix of the model (Menke, 1984).

The capabilities of the ray geometry and model parameter grid to resolve the velocity perturbations can be formally estimated by resolution matrix (Menke, 1984):

$$\mathbf{R} = (\mathbf{G}^{\mathrm{T}}\mathbf{W}_{\mathrm{D}}\mathbf{G} + \varepsilon^2\mathbf{W}_{\mathrm{M}})^{-1}\mathbf{G}^{\mathrm{T}}\mathbf{W}_{\mathrm{D}}\mathbf{G}. \quad (3)$$

SED
6, 1–36, 2015

Best results for resolution estimates, however, are obtained by synthetic data testing in combination with hit count, derivative weighted sums, and resolution matrix (Kissling, 1988).

4.1 Model parameterization and regularization

The POLENET/LAPNET study area is approximately 550 km in east-west direction and 600 km in north-south direction. For this study area we selected an 80 km × 80 km × 60 km inversion grid. The horizontal size of the cells is slightly larger than the average distance between stations to guarantee at least one station for each surface cell within the array space. Thus, the minimum dimension of a resolvable anomalous body beneath POLENET/LAPNET array is approximately 100 km. The uppermost 60 km are mostly made of crust and are not included in the high-resolution teleseismic inversion (e.g., Arlitt et al., 1999). In the case of real data, a priori crustal corrections are applied to travel time residuals (see Sect. 4.2). For the inversion of synthetic data (see Sect. 4.3) no crustal correction was applied as the crustal layers were assumed to have velocities according to the ~~IASP91~~ reference model. The first layer inverted for below 60 km crustal layer is 40 km thick and all deeper layers are of thickness 60 km. For better performance of the ray tracer, the study volume was surrounded on all sides and ~~on~~ bottom with large cells of respective ~~IASP91~~ velocities that were kept fixed during inversion. The P-wave velocities of the initial model correspond to the ~~IASP91~~ reference model. Because of the uneven ray geometry the kernel matrix (**G** in Eq. 1) can be singular and needs to be regularized. The regularization can be done by selecting appropriate damping value for the dataset (ε^2 in Eq. 2). We analysed the effect of the damping values by performing multiple inversions with different damping values both with synthetic data and real data to find the best damping value for our data set. The final damping value 70 was selected by investigating the trade-off curve between model and data variance (see Fig. 5 for the trade of curve of the real data and Fig. 6 for examples of the crustal corrected residuals).

SED
6, 1–36, 2015

4.2 Crustal correction model

Due to high angles of incident and subsequent near-lack of cross firing, teleseismic rays are largely incapable to resolve upper lithosphere structure such as Moho topography and 3-D crustal velocity variations. Lateral variation of crustal structure, however, may significantly affect travel times of teleseismic rays (Arlitt et al., 1999). Hence, when illuminating with high-resolution teleseismic tomography the structures at upper mantle depths, it is necessary to apriori correct the data for the effect of crustal structures as documented for southern Finland by Sandoval et al. (2003). A new map of the crustal thickness was established by Silvennoinen et al. (2014) based on previous and new controlled source seismic and receiver function results in our study area. This map in combination with an averaged 1D-velocity-depth function is used in this study to construct a 3-D crustal model for the purpose of correcting travel times for crustal effects.

The 3-D crustal model used in this study was established by using Bloxer software (https://wiki.oulu.fi/display/~mpi/Block+model+maintenance). Bloxer is software designed to build 3-D block models with different parameters (density, seismic velocity, magnetization etc.). The Moho depth map by Silvennoinen et al. (2014) was imported to Bloxer. All blocks below the Moho to a maximal model depth of 60 km were given a P-wave velocity value 8.05 km s^{-1} that is the P-wave velocity ~~at~~ uppermost mantle of ~~IASP91~~ reference model.

As our study area has not enough P-wave velocity information available to estimate a true 3-D distribution of seismic velocities in the crust between CSS profiles, we used an average P-wave velocity for crustal depths defined from major refraction seismic profiles, namely FENNOLORA (Guggisberg, 1986; Guggisberg et al., 1991; Luosto and Korhonen, 1986) in Sweden, POLAR (Luosto et al., 1989; Janik et al., 2009) in Finland, and PECHENGA-KOSTOMUKSHA (Azbel et al., 1989; Azbel and Ionkis, 1991; Azbel et al., 1991) in Russia. A map of crustal correction times for vertical incident rays arriving at each station is shown in Fig. 6a. The crustal effect established by Sandoval

SED
6, 1–36, 2015

et al. (2003) for southern and central Finland have almost perfect fit with the crustal effect established in this study for the overlapping southern part of our study area (south of 65.5° N).

To evaluate the effect of this "pseudo-3-D" model with averaged velocity-depth function and locally variable Moho depths on travel times in comparison with the effect of local 2-D velocity distribution derived from a wide-angle reflection and refraction profile we calculated the travel times trough our model to the depth of 70 km along the POLAR profile (Janik et al., 2009). This profile is located near the center of our study area. We found the effect of local crustal velocity-depth variations to be minor compared to the effect of the variation in Moho depth (see Fig. 6b).

Figure 7 shows an example of crustal corrected travel time residuals for the same stations that were used in Fig. 4.

4.3 Resolution and the synthetic tests

To evaluate the reliability or the tomography inversion results, it is necessary to identify which parts of the resulting model are resolved well and which parts may contain artefacts caused by the method. In our study we analysed the resolution using the diagonal elements of the resolution matrix and using a series of synthetic tests.

The resolution matrix can be used to evaluate the capabilities of the ray geometry and model parameter grid to resolve the velocity perturbations by inversion of the travel time data set. The diagonal elements of the resolution matrix correspond to a-posteriori variances of the model parameters (Menke, 1984). Therefore, the closer the diagonal element is to a value 1.0, the better the correspondent model parameter is resolved. Based on this criterion, the resolution is fair to reasonably good below the station array at all depths. Figure 8 shows the diagonal elements at two vertical and two horizontal sections though our study volume. The best resolution is below the centre of the array in the depth range of less than 360 km (see Fig. 8). The area with best resolution moves eastward at larger depths, corresponding the region of most cross firing from events in NE, E, and SE (see Fig. 8b). The resolution is generally better beneath the eastern

SED
6, 1–36, 2015

part of the study area than the western part of the study area. This is understandable as the stations ~~at~~ central and eastern part of the study area recorded more events than stations in the western part and the most common back azimuth direction pointed to the east. As a consequence, the number of rays crossing the cells in the western part of the study area, especially from south to north, was smaller and the ray coverage sparser.

The sensitivity of our dataset to velocity heterogeneities in the upper mantle was tested with the "checkerboard" test. We constructed a model consisting of alternating positive and negative anomalies placed regularly through the study area in both vertical and horizontal directions. The magnitudes of the anomalies were ±2 % compared to the ~~IASP91~~ reference model and the anomaly size was 160 km × 160 km × 120 km or 2 × 2 × 2 cells in the inversion grid. Between the anomalies we left layers with no velocity perturbations as suggested by Sandoval et al. (2004). Examples of the model at two depths (120 and 360 km) are shown in Fig. 9.

A synthetic dataset was calculated using this model and the ray parameters of the real data set, and the resulting synthetic data set was inverted back to a velocity model. In horizontal direction the anomalies were generally well recovered below the station array at all depths. Also in the vertical direction the recovery was good in the central and eastern parts of the study area. In the western part, however, there was some smearing in the north-south direction. Figure 9 compares the model used for computing the synthetic data set and the results after inversion with our selected damping value at selected depths of 120 and 360 km as well as 2 horizontal sections.

Additionally the resolution was evaluated using synthetic tests with different structures simulating large-scale anomalies in the upper mantle. We speculated that there could be such structure in the upper mantle roughly below the Belomorian Mobile Belt (see Fig. 1). That is why both tests have an anomalous body there and an additional body to help us visualize how anomalies can affect each other. The synthetic test models and results are shown in Fig. 10. From the results we can see that while the anomalies are recovered quite well there is some leakage both up- and down-ward. Similarly

SED
6, 1–36, 2015

to checkerboard tests, we see that the resolution in western part of the study area is not as good as in the eastern part. In the areas with fairly good resolution leakage may generally extends into the next layer up or down from the anomalous body, while in areas with poor resolution the leakage can extend to 2 layers (i.e., up to 120 km). From the test (Fig. 10) we can also see that we obtain slight positive anomalies around the negative anomalous body and vice versa marking an "overswinging" effect Kissling et al. (2001).

5 Results and discussion

The main results of inversion with the real data are shown in Figs. 11 and 12. Our study revealed highly heterogeneous lithospheric mantle beneath the northern Fennoscandian Shield, without any large high P-wave velocity area that may indicate presence of thick depleted lithospheric "keel" revealed beneath southern part of the shield in Sweden (Shomali et al., 2006) and beneath the SVEKALAPKO study area (Sandoval et al., 2004) and in some other shield areas (e.g., Pasyanos and Nyblade, 2007; Priestley et al., 2008; Villemaire et al., 2012). As can be seen, P-wave velocities in our model are generally close to the reference IASP91 model, this is in agreement with the recent result of joint analysis of P- and S-wave receiver functions by (Vinnik et al., 2015). They showed that absolute average values of seismic velocities in the lithospheric mantle beneath southern Finland are generally higher than those beneath the northern Finland. Because of limitations of the data, they did not analyse the lateral heterogeneities in the lithospheric mantle. However, in our model we can recognize several high velocity anomalies in the upper part of the lithospheric mantle (down to depths of about 120–200 km) that spatially correlate with the Karelian, Kola and Norrbotten cratons (Fig. 11a, b). We interpret these high-velocity anomalies as non-reworked fragments of cratonic lithosphere preserved since the Archaean.

The non-reworked part of the Karelian craton can be recognized as a fast velocity anomaly (+3 %) from the Moho down to a depth of about 160 km. Below this depth we

SED
6, 1–36, 2015

observed velocities lower than those in the reference model. At the margin of the Kola craton we also see a positive (+3.5 %) anomaly roughly down to 180 km. Below it the velocity values are close to those from the reference model (Fig. 11d). The Norrbotten Craton is also seen as a high velocity anomaly (+1.5 %) starting from the Moho down to a depth of about 200 km (Fig. 11). These upper mantle heterogeneities can be explained by three major factors, namely temperature variations, compositional variations or seismic anisotropy.

Seismic anisotropy beneath the POLENET/LAPNET area was studied independently by Plomerová et al. (2011) and Vinnik et al. (2014). Plomerová et al. (2011) analysed the relative P-wave travel-time deviations of selected teleseismic events and lateral variations of shear-wave splitting. Their results demonstrate the lithosphere of the study area consists of distinctive domains of anisotropic structures. One of their foundings was that the patterns related to the Proterozoic-Archean transition zone in central Finland continued to POLENET/LAPNET study area. The Archean mantle block interpreted by Plomerová et al. (2011) is collocated with the south-eastern upper mantle high velocity anomaly of our model. Vinnik et al. (2014) analysed the southern half of the POLENET/LAPNET study area using joint inversion of P-wave receiver functions and SKS recordings. They obtained an averaged depth distribution of the magnitude and azimuthal direction of the anisotropy in the area. They found an anisotropic layer with approximate S-wave anisotropy of 2.5 % from below Moho to approximately 110 km with fast direction of 40–60° as well as another, slightly less anisotropic layer with same azimuthal direction starting from approximately 220 km. Above this lower layer they modelled another anisotropic layer with contrasting azimuthal direction of 110°. Radial anisotropy found by Vinnik et al. (2014) does not influence significantly travel times of teleseismic P-waves, propagating in sub-vertical direction.

As shown by Lee (2003), James et al. (2004) and Schutt and Lesher (2006), compositional variations between depleted in Fe and more fertile mantle peridotites can explain up to 1–2 % velocity anomalies of P-wave velocities. In order to explain larger anomalies, one would need the combined effect of major element chemistry and tem-

SED
6, 1–36, 2015

perature, as shown by Hieronymus and Goes (2010). That is why the lowered seismic velocities in the lithospheric mantle in our study area are most probably due to the combined effect of more fertile composition and generally higher temperature.

The most significant feature seen in the velocity model is a large negative velocity anomaly (up to −3.5 %) in the central part of our study area that can be followed down to a depth of 160–200 km (Fig. 11). In the upper part of the model this low-velocity area separates three high-velocity region corresponding to the cratons and it extends to the greater depth below the Karelian craton (Fig. 11b, c, d). As is shown in several previous studies (e.g., Pedersen et al., 2013; Plomerová and Babuška, 2010; Lebedev et al., 2009), the lithospheric thickness in POLENET/LAPNET study area in northern Fennoscandia must be at least roughly 150 km, which makes it unlikely the upper boundary of the low velocity anomaly seen in our model at depth shallower than 100 km ~~were~~ the lithosphere-astenosphere boundary. In Fig. 13 we show a north-south directed cross-section through a model based on surface waves by Pedersen et al. (2013) together with the location of the low velocity zone found in our study.

The low velocity zone is spatially overlapping in the East with the Kola alkaline province (see Fig. 14), in which the crust has been intruded by alkaline magmas (Downes et al., 2005) during several metasomatic events. Kempton et al. (1995) proposed that at least one of them was ancient, while the latest occurred in Devonian. The same events would result also in extensive reworking and refertilization of the originally depleted Archean mantle keel, while the latest Devonian magmatism would explain also higher mantle temperatures.

On the other hand, the area of low seismic velocities in the central part of the array separates Norrbotten, Kola and Karelian Cratons from each other and is spatially correlating with the northern part of the 1.9–1.8 Ga N–S trending Baltic-Bothnia Megashear (BBMS) stretching below the Baltic Sea and Gulf of Bothnia and continuing to the Caledonides in Norway (Berthelsen and Marker, 1986, see Fig. 13;). The northern part of the BBMS was later named Pajala shear zone by Kärki et al. (1993). This shear zone is about 40 km wide represented by a complex set of N–S striking shear and thrust

SED
6, 1–36, 2015

zones. Lahtinen et al. (2015) proposed that the Pajala shear zone originated as a divergent plate boundary due to collision of two Archean continental units (Norrbotten and Karelian), and it was multiply reactivated after continental collision with both lateral and vertical movements before 1.83 Ga. The vertical seismic velocity distribution in the upper mantle obtained in our model (e.g. low velocity over high velocities similar to that revealed by Bruneton et al. (2004) and Sandoval et al. (2004) (see Fig. 14), we suggest that the Pajala shear zone may continue to the south beneath the Gulf of Bothnia, as was originally proposed by Berthelsen and Marker (1986).

However, the metasomatic processes and refertilization of the upper mantle in the Palaoproterozoic alone would not produce such low seismic velocities as we observed in our model and combined effect of temperature and composition would be necessary (Hieronymus and Goes, 2010). Thus we may speculate that since the Palaeoproterozoic the whole BBMS was reactivated by a later tectonothermal event (or multiple events), during which the cratonic lithosphere was partly destroyed. The time of those events is not clear, but it could occur the same time with the Paleozoic post-collisional akaline magmatism in the Kola alcaline province caused by a plume activity (Marty et al., 1998; Downes et al., 2005; Kogarko et al., 2010).

Acknowledgements. The authors would like to thank the staff of both Sodankylä geophysical observatory, Institute of G geophysics of ETH Zürich and Institute of geophysics of the Academy of sciences of the Czech Republic for all technical help during this study. Hanna Silvennoinen would also like to thank Finnish Academy of Science and Letters and Apteekin rahasto for funding her during her part of this study. The POLENET/LAPNET working group members are Elena Kozlovskaya, Helle Pedersen, Jaroslava Plomerová, Ulrich Achauer, Eduard Kissling, Irina Sanina, Teppo Jämsén, Hanna Silvennoinen, Catherine Pequegnat, Riitta Hurskainen, Robert Guiguet, Helmut Hausmann, Petr Jedlicka, Igor Aleshin, Ekaterina Bourova, Reynir Bodvarsson, Evald Brückl, Tuna Eken, Pekka Heikkinen, Gregory Houseman, Helge Johnsen, Elena Kremenetskaya, Kari Komminaho, Helena Munzarova, Roland Roberts, Bohuslav Ruzek, Hossein Shomali, Johannes Schweitzer, Artem Shaumyan, Ludek Vecsey and Sergei Volosov.

References

Aki, K., Christoffersson, A., and Husebye, E.: Determination of the three-dimensional seismic structure of the lithosphere, J. Geophys. Res., 82, 277–296, 1977. 7

Arlitt, R., Kissling, E., and Ansorge, J.: Three-dimensional crustal structure beneath the TOR array and effects on teleseismic wavefronts, Tectonophysics, 314, 309–319, 1999. 7, 8, 9

Azbel, I. and Ionkis, V.: The analysis and interpretation of wave fields on Soviet and Finnish DSS profiles, in: Structure and dynamics of the Fennoscandian lithosphere, edited by Korhonen, H. and Lipponen, A., Institut of Seismology, University of Helsinki, Helsinki, Finland, 21–30, 1991. 9

Azbel, I., Buyanov, A., Ionkis, V., Sharov, N., and Sharova, V.: Crustal structure of the Kola-Peninsula from inversion of deep seismic-sounding data, Tectonophysics, 162, 78–99, 1989. 9

Azbel, I., Yegorkin, A., Ionkis, V., and Kagaloval, L.: Pecularities of the Earth's crust deep structure along the Nikel-Umbozero-Ruchýi profile, Investigation of the Earth's continental lithosphere with complex seismic methods, Institut of Mines, St. Petersburg, Russia, 1991. 9

Berthelsen, A. and Marker, M.: 1.9–1.8 Ga old strike-slip megashear in the Baltic Shield, and their plate tectonic implications, Tectonophysics, 128, 163–181, 1986. 14, 15

Bruneton, M., Pedersen, H., Farra, V., Arndt, N., Vacher, P., and SVEKALAPKO Seismic Tomography Working Group: Complex lithospheric structure under the central Baltic Shield from surface wave tomography, J. Geophys. Res., 109, B10303, doi:10.1029/2003JB002947, 2004. 15, 36

Clifford, T.: Tectono-metallogenic units and metallogenic provinces of Africa, Earth Plan. Sci. Lett., 421–434, 1966. 3

Daly, J. S., Balagansky, V. V., Timmerman, M. J., and Whitehouse, M. J.: The Lapland-Kola orogen: Palaeoproterozoic collision and accretion of the northern Fennoscandian lithosphere, in: European Lithosphere Dynamics, edited by: Gee, D. G. and Stephenson, R. A., Geol. Soc. London, Mem. Ser., 32, 579–598, 2006. 4

Debayle, E. and Ricard, Y.: A global shear velocity model of the upper mantle from fundamental and higher Rayleigh mode measurements, J. Geophys. Res., 117, B10308, doi:10.1029/2012JB009288, 2012. 35

SED
6, 1–36, 2015

Downes, H., Balaganskaya, E., Beard, A., Liferovich, R., and Demaiffe, D.: Petrogenetic processes in the ultramafic, alkaline and carbonatitic magmatism in the Kola Alkaline Province: A review, Lithos, 85, 48–75, 2005. 5, 14, 15

Eken, T., Shomali, H., Roberts, R., and Bodvarsson, R.: Upper mantle structure of the Baltic Shield below the Swedish National Seismological Networks (SNSN) resolved by teleseismic tomography, Geophys. J. Int., 169, 617–630, 2007. 4

Evans, J. and Achauer, U.: Teleseismic velocity tomography using the ACH method: theory and application to continental scale studies, in: Seismic Tomography, edited by: Iyer, H. and Hirahara, K., Chapman and Hall, London, UK, 319–360, 1993. 7

Guggisberg, B.: Eine zweidimensionale refraktionseismische Interpretation der Geschwindigkeits-Tiefen-Struktur des oberen Erdmantels unter dem Fennoskandischen Schild (Projekt FENNOLORA), PhD thesis, ETH, Zürich, Switzerland, 1986. 9

Guggisberg, B., Kaminski, W., and Prodehl, C.: Crustal structure of the fennoscandian shield – a traveltime interpretation of the long-range Fennolora seismic refraction profile, Tectonophysics, 195, 105–137, 1991. 9

Hieronymus, C. and Goes, S.: Complex cratonic seismic structure from thermal models of the lithosphere: effects of variations in deep radiogenic heating, Geophys. J. Int., 180, 999–1012, 2010. 14, 15

Hjelt, S.-E., Korja, T., Kozlovskaya, E., Lahti, I., Yliniemi, J., and BEAR and SVEKALAPKO Working Groups: Electrical conductivity and seismic velocity structures of the lithosphere beneath the Fennoscandian Shield, in: European Lithosphere Dynamics, edited by: Gee, D. and Stephenson, R., Geol. Soc. London, Mem. Ser., 32, 2006. 6

James, D., Boyd, F., Schutt, D., Bell, D., and Carlson, R.: Xenolith constraints on seismic velocities in the upper mantle beneath southern Africa, Geochem. Geophys. Geosys., 5, Q01002, doi:10.1029/2003GC000551, 2004. 13

Janik, T., Kozlovskaya, E., Heikkinen, P., Yliniemi, J., and Silvennoinen, H.: Evidence for preservation of crustal root beneath the Proterozoic Lapland-Kola orogen (northern Fennoscandian shield) derived from P and S wave velocity models of POLAR and HUKKA wide-angle reflection and refraction profiles and FIRE4 reflection transect, J. Geophys. Res.-Sol. Ea., 114, B06308, doi:10.1029/2008JB005689, 2009. 9, 10, 28

Janutyte, I., Kozlovskaya, E., Majdanski, M., Voss, P. H., Budraitis, M., and PASSEQWorking Group: Traces of the crustal units and the upper-mantle structure in the southwestern part of the East European Craton, Solid Earth, 5, 821–836, doi:10.5194/se-5-821-2014, 2014. 3

SED
6, 1–36, 2015

Kärki, A., Laajoki, K., and Luukas, J.: Major Palaeoproterozoic shear zones of the central Fennoscandian Shield, Precambrian Res., 64, 207–223, 1993. 14
Kempton, P., Downes, H., Sharkov, E., Vetrin, V., Ionov, D., Carswell, D., and Beard, A.: Petrology and geochemistry of xenoliths from the Northern Baltic shield: evidence for partial melting and metasomatism in the lower crust beneath an Archaean terrane, Lithos, 36, 157–184, 1995. 14
Kennett, B. and Engdahl, E.: Traveltimes for global earthquake location and phase identification, Geophys. J. Int., 105, 429–465, 1991. 5, 7, 26, 34
Kissling, E.: Geotomography with local earthquake data, Rev. Gephysics, 26, 659–698, 1988. 6, 8
Kissling, E., Husen, S., and Haslinger, F.: Model parameterization in seismic tomography: a choise of consequence for the solution quality, Phys. Earth Planet. In., 123, 89–101, 2001. 12
Kogarko, L., Lahaye, Y., and Brey, G.: Plume-related mantle source of super-large rare metal deposits from the Lovozero and Khibina massifs on the Kola Peninsula, Eastern part of Baltic shield: Sr, Nd and Hf isotope systematics, Mineral. Petrol., 98, 197–208, 2010. 15
Koistinen, T., Stephens, M. B., Bogatchev, V., Nordgulen, Ø., Wennerström, M., and Korhonen, J.: Geological map of Fennoscandian shield, scale 1 : 2 000 000, Geological Surveys of Finland, Norway and Sweden and the North-West Department of Natural Resources of Russia, 2001. 23
Lahtinen, R., Garde, A. A., and Melezhik, V. A.: Paleoproterozoic evolution of Fennoscandia and Greenland, Episodes, 31, 1–9, 2008. 4, 5
Lahtinen, R., Huhma, H., Lahaye, Y., Jonsson, E., Manninen, T., Lauri, L., Bergman, S., Hellström, F., Niiranen, T., and Nironen, M.: New geochronological and Sm-Nd constraints across the Pajala shear zone of northern Fennoscandia: Reactivation of a Paleoproterozoic suture, Precambrian Res., 256, 102–119, 2015. 5, 15, 23
Laznicka, P.: Giant metallic deposits – A century of progress, Ore Geol. Rev., 62, 259–314, 2014. 3
Lebedev, S., Boonen, J., and Trampert, J.: Seismic structure of Precambrian lithosphere: New constraints from broad-band surface-wave dispersion, Lithos, 109, 96–111, 2009. 14
Lee, C.-T.: Compositional variation of density and seismic velocities in natural peridotites at STP conditions: implications for seismic imaging of compositional heterogeneities in the upper mantle, J. Geophys. Res., 108, 2441, doi:10.1029/2003JB002413, 2003. 13

SED
6, 1–36, 2015

Lippitsch, R., Kissling, E., and Ansorge, J.: Upper mantle structure beneath the Alpine orogen from high-resolution teleseismic tomography, J. Geophys. Res., 108, 2376, doi:10.1029/2002JB002016, 2003. 7

Luosto, U. and Korhonen, H.: Crustal structure of the baltic shield based on off – Fennolora refraction data, Tectonophysics, 128, 183–208, 1986. 9

Luosto, U., Flueh, E., C.-E., L., and POLAR Working group: The crustal structure along the POLAR profile from seismic refraction investigation., Tectonophysics, 162, 51–85, 1989. 9

Marty, B., Tolstikhin, I., Kamensky, I., Nivin, V., Balaganskaya, E., and Zimmerman, J.-L.: Plume-derived rare gases in 380 Ma carbonatites from the Kola region (Russia) and the argon isotopic composition in the deep mantle, Earth Plan. Sci. Lett., 164, 179–192, 1998. 15

Menke, W.: Geophysical Data Analysis: Discrete Inverse Theory, International Geophysical Series, Academic Press, London, UK, 45, 1984. 7, 10

Mole, D., Fiorentini, M. L., Cassidy, K. F., Kirkland, C. L., Thebaud, N., McCuaig, T. C., Doublier, M. P., Duuring, P., Romano, S. S., Maas, R., Belousova, E. A., Barnes, S. J., and Miller, J.: Crustal evolution, intra-cratonic architecture and the metallogeny of an Archaean craton, Special Publications, Geol. Soc. London, 393, 23–80, doi:10.1144/SP393.8, 2014. 3

Pasyanos, M. and Nyblade, A.: A top to bottom lithospheric study of Africa and Arabia, Tectonophysics, 444, 27–44, 2007. 12

Pedersen, H., Debayle, E., Maupin, V., and the POLENET/LAPNET Working Group: Strong lateral variations of lithospheric mantle beneath cratons – Example from the Baltic Shield, Earth Plan. Sci. Lett., 383, 164–172, 2013. 14, 35

Plomerová, J. and Babuška, V.: Long memory of mantle lithosphere fabric – European LAB constrained from seismic anisotropy, Lithos, 120, 131–143, 2010. 14

Plomerová, J., Babuška, V., Vecsey, L., Kozlovskaya, E., Raita, T., and SSTWG: Proterozoic-Archean boundary in the upper mantle of eastern Fennoscandia as seen by seismic anisotropy, J. Geodyn., 41, 400–410, 2006. 6

Plomerová, J., Vecsey, L., Babuška, V., and LAPNET Working Group: Domains of Archean mantle lithosphere deciphered by seismic anisotropy – inferences from the LAPNET array in northern Fennoscandia, Solid Earth, 2, 303–313, doi:10.5194/se-2-303-2011, 2011. 4, 13

Priestley, K., McKenzie, D., Debayle, E., and Pilidou, S.: The African upper mantle and its relationship to tectonics and surface geology, Geophys. J. Int., 175, 1105–1126, 2008. 12

SED
6, 1–36, 2015

Sandoval, S., Kissling, E., Ansorge, J., and the SVEKALAPKO Seismic Tomography Working Group: High-resolution body wave tomography beneath the SVEKALAPKO array – Part I: A priori three-dimensional crustal model and associated traveltime effects on teleseismic wave fronts, Geophys. J. Int., 153, 75–87, 2003. 9

Sandoval, S., Kissling, E., Ansorge, J., and SVEKALAPKO STWG: High-resolution body wave tomography beneath the SVEKALAPKO array: II. Anomalous upper mantle structure beneath the central Baltic Shield, Geophys. J. Int., 157, 200–214, 2004. 3, 7, 11, 12, 15, 36

Schutt, D. and Lesher, C.: The effects of melt depletion on the density and seismic velocity of garnet and spinel lherzolite, J. Geophys. Res., 111, B05401, doi:10.1029/2003JB002950, 2006. 13

Shomali, Z., Roberts, R., Pedersen, L., and TOR Working Group: Lithospheric structure of the Tornquist Zone resolved by nonlinear P and S teleseismic tomography along the TOR array, Tectonophysics, 416, 133–149, 2006. 3, 12

Silvennoinen, H., Kozlovskaya, E., Kissling, E., Kosarev, G., and POLENET/LAPNET working group: A new Moho boundary map for northern Fennoscandian shield based on combined controlled-source seismic and receiver function data, GeoResJ, 1–2, 19–32, 2014. 9

Snyder, D., Rondenay, S., Bostock, M., and Lockhart, G.: Mapping the mantle lithosphere for diamond potential using teleseismic methods, Lithos, 77, 859–872, 2004. 3

Steck, L. K. and Prothero, W.: A 3-D ray-tracer for teleseismic body-wave arrival-times, B. Seismol. Soc. Am., 81, 1332–1339, 1991. 7

Trampert, J. and Van der Hilst, R.: Towards a quantitative interpretation of global seismic tomography, Geophysical Monograph, American Geophysical Union, 160, 2005. 2

Villemaire, M., Darbyshire, F., and Bastow, I.: Evolution of the mantle from Archean to Phanerozoic and its modification during subsequent hotspot tectonism : seismic evidence from eastern North America, J. Geophys. Res., 117, B12302, doi:10.1029/2012JB009639, 2012. 12

Vinnik, L., Oreshin, S., Makeyeva, L., Peregoudov, D., Kozlovskaya, E., and POLENET/LAPNET Working Group: Anisotropic lithosphere under the Fennoscandian shield from P receiver functions and SKS waveforms of the POLENET/LAPNET array, Tectonophysics, 628, 45–54, 2014. 4, 13

Vinnik, L., Oreshin, S., Kozlovskaya, E., Kosarev, G., Piiponen, K., and Silvennoinen, H.: Lithosphere and asthenosphere under central Fennoscandia from P- and S-wave receiver functions, Earth Plan. Sci. Lett., submitted, 2015. 4, 12

SED
6, 1–36, 2015

Weiland, C., Steck, L., Dawson, P., and Korneev, V.: Nonlinear teleseismic tomography at Long Valley caldera, using three-dimensional minimum travel time ray tracing, J. Geophys. Res., 100, 20379–20390, 1995. 7

Woodard, J.: Genesis and Emplacement of Carbonatites and Lamprophyres in the Svecofennian Domain, PhD thesis, University of Turku, Turku, Finland, 2010. 5

SED

6, 1–36, 2015

Table 1. The travel time data quality classes. The table shows the data quality classes, the corresponding error estimates and the number of travel time residual in the quality class for POLENET/LAPNET data, SVEKALAPKO data and the total. The lowermost row shows the total number of travel time residuals over all quality classes for both projects and finally the total number of travel time residuals in our database.

Quality class	Error estimate [s]	Number of POLENET/LAPNET residuals	Number of SVEKALAPKO residuals	Total number of residuals
1	±0.1	2572	239	2811
2	±0.2	430	85	515
3	±0.4	165	35	200
Total		3167	359	3526

SED
6, 1–36, 2015

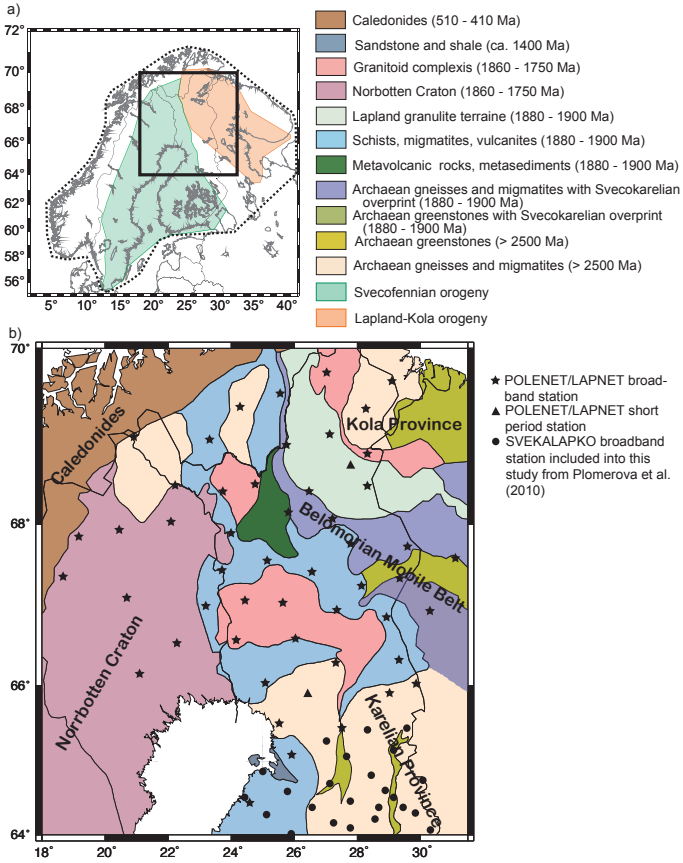

Figure 1. The map of the study area. **(a)** Simplified map of orogenies (based on Lahtinen et al. (2015) in northern Fennoscandia. The Fennoscandian crustal block is outlined by black dotted line and our study area a rectangle. **(b)** The simplified geological map is based on 1 : 2 000 000 geological map of Fennoscandia (Koistinen et al., 2001). The seismic stations are shown with black stars, triangles and dots and main geological provinces are named.

SED
6, 1–36, 2015

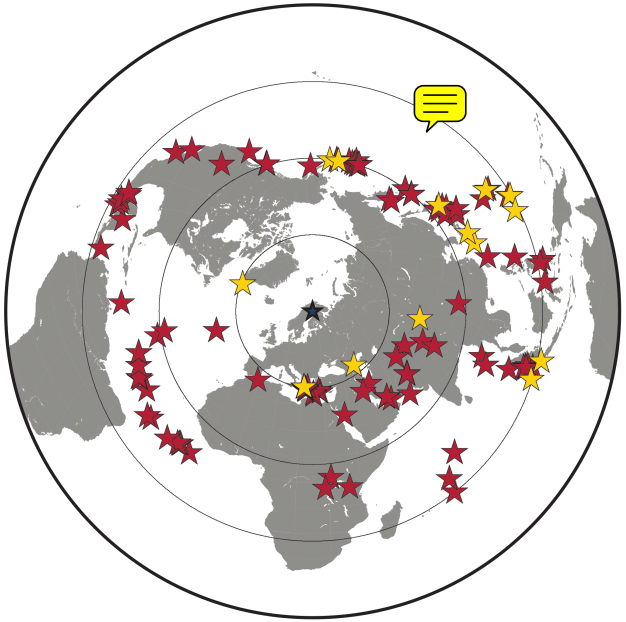

Figure 2. Location of the 111 teleseismic events used as sources for the tomography study. The centre of our array is shown with blue star while events recorded by POLENET/LAPNET array are shown with red stars (96 events) and by SVEKALAPKO project with yellow stars (15 events).

SED
6, 1–36, 2015

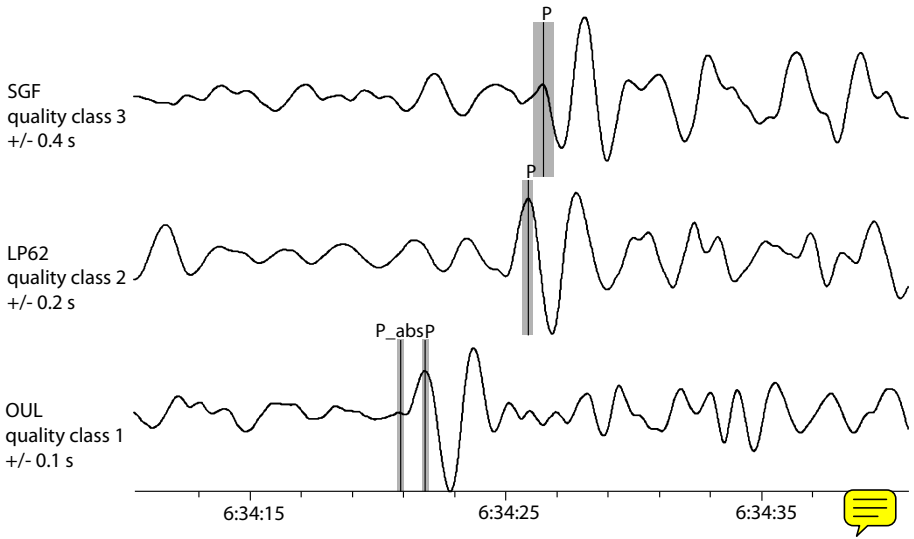

Figure 3. Example traveltime picks of different quality from same event observed at three different stations. The recorded waveforms have been filtered with the WWSSN short period simulation filter. The travel time observation from the station OUL was attributed a quality class 1, the one from station LP62 a quality class 2 and from station SGF a quality class 3. For OUL the absolute travel (P_{abs}) time was picked as well as the relative travel time (P). For each pick the timing uncertainty estimate of the quality class is shown with grey rectangle.

SED
6, 1–36, 2015

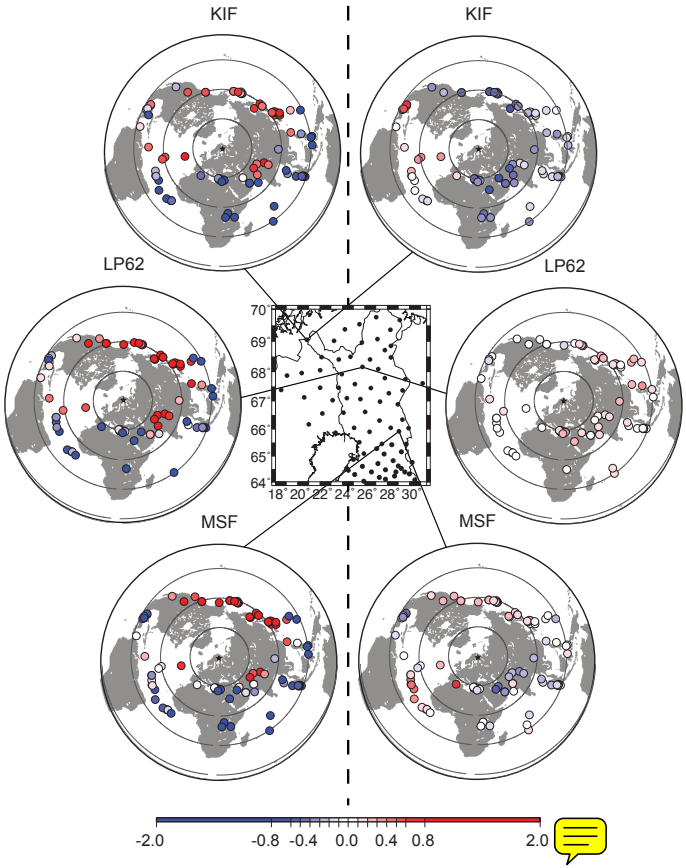

Figure 4. Distribution of traveltime residuals relative to standard Earth model ~~IASP91~~ (Kennett and Engdahl, 1991) at three example stations selected from different parts of POLENET/LAPNET array. The observed residuals are on the left hand side and the residuals after the average over all stations for each event has been removed are on right hand side.

SED
6, 1–36, 2015

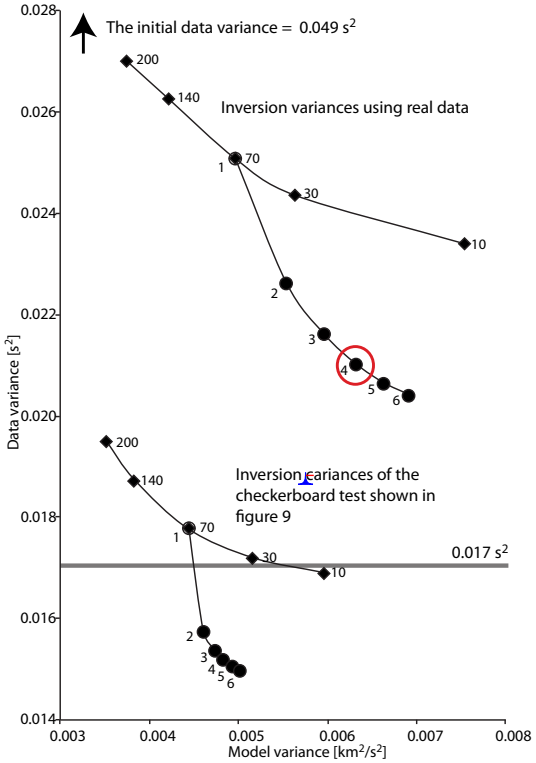

Figure 5. A comparison between data and model variance with different damping values. The selected damping value was first found using one inversion round only and the results are shown with diamonds with the damping value used shown on the right side of the symbols. The number of iterations was also optimized (dots with the number of iterations marked to their left side) for the selected damping value 70. The final number of iterations, 4, is marked with red circle. The grey line denotes the overall data uncertainty, 0.017 s^2, calculated as the average of all observations.

SED
6, 1–36, 2015

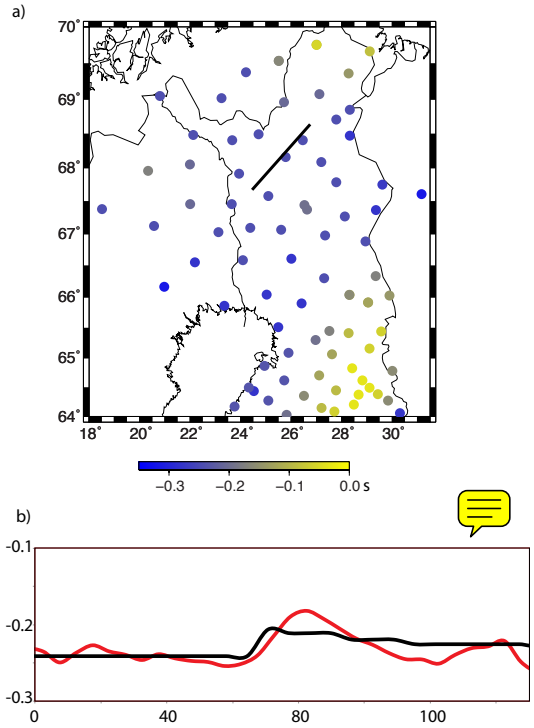

Figure 6. Crustal correction map. Panel **(a)** shows crustal correction values for all of the station. The values are based on a travel time of a vertical seismic ray travelling through the crustal correction model. Panel **(b)** shows the comparison of the travel times through semi-2-D crustal correction model used in this study (black line) and southern part of POLAR wide-angle reflection and refraction profile (red line, Janik et al., 2009). The location of the comparison is shown as a black line in panel **(a)**.

SED
6, 1–36, 2015

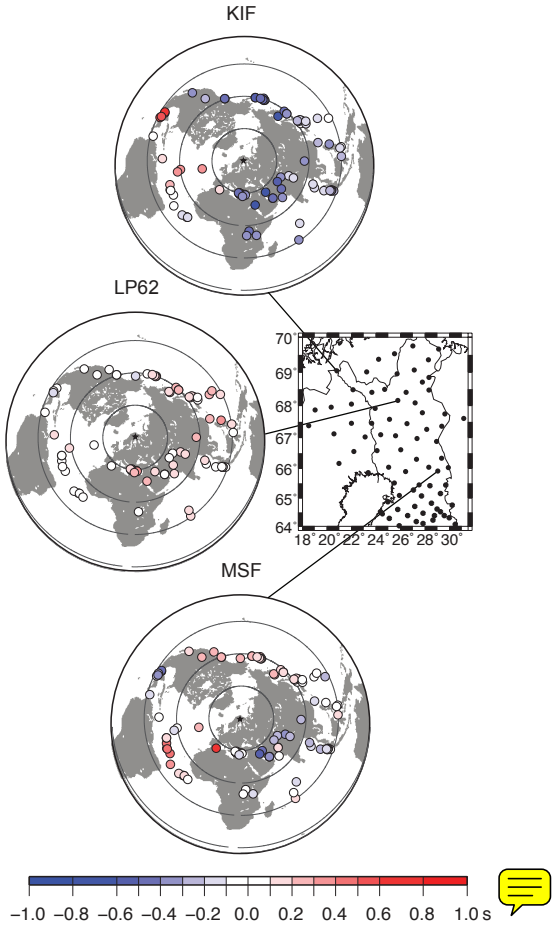

Figure 7. Distribution of crustal corrected travel time residuals at few example stations from different parts of POLENET/LAPNET array.

SED
6, 1–36, 2015

POLENET/LAPNET teleseismic P-wave traveltime tomography model

H. Silvennoinen et al.

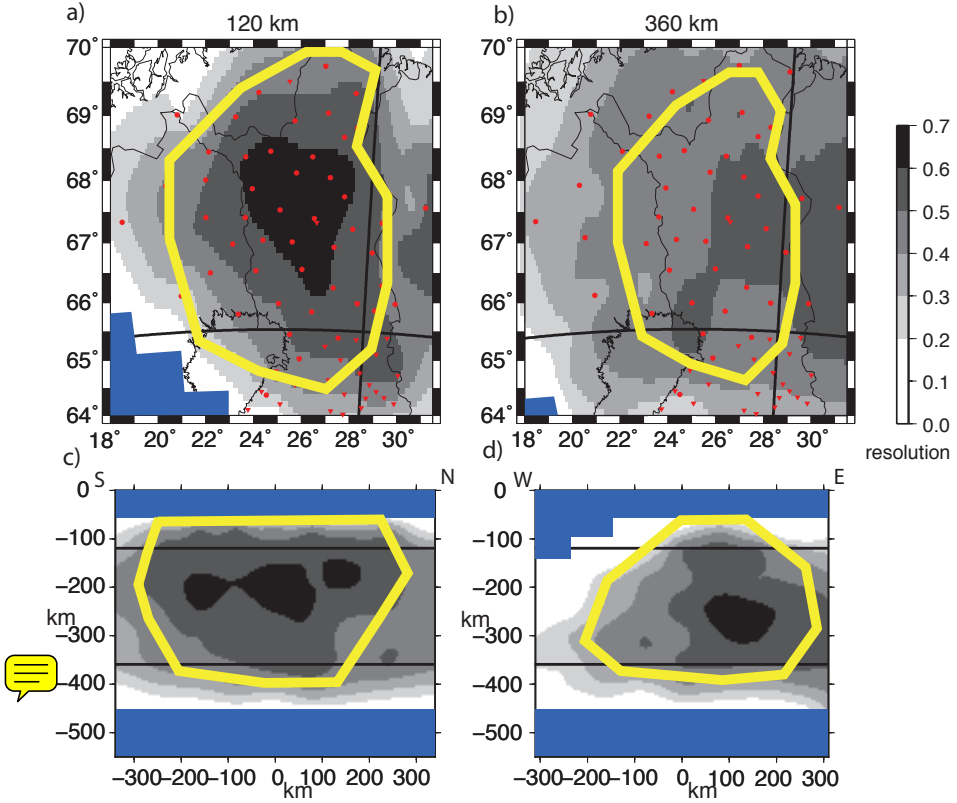

Figure 8. Diagonal elements of the resolution matrix (RDE). **(a)** and **(b)** show RDE for horizontal layers at depths of 120 and 360 km, respectively, **(c)** RDE distribution along a north-south directed vertical section, and **(d)** RDE along a west-east directed vertical section. The locations of the vertical sections are marked in horizontal sections with black lines and vice versa. The blue blocks show areas that were not inverted, as there was no data available. Red dots and triangles show the locations of POLENET/LAPNET and SVEKALAPKO stations, respectively.

SED
6, 1–36, 2015

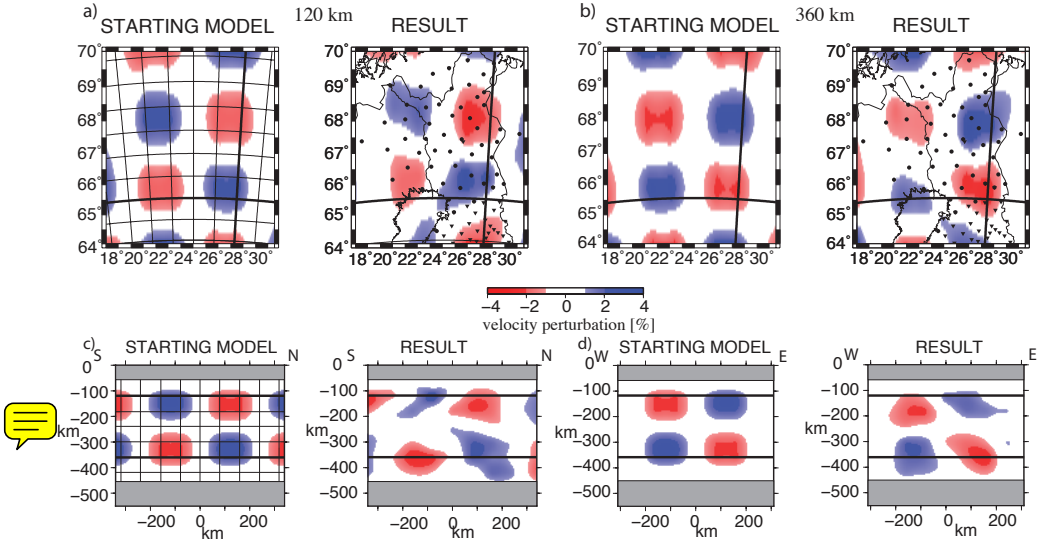

Figure 9. Checkerboard test results. Two horizontal sections are shown at the depths of 120 and 360 km (**a** and **b**) as well as two vertical sections, one in SN direction **(c)** and one in EW direction **(d)**. For each section both the model used to compute the synthetic data set and the result after inversion are shown. The model plots of **(a)** and **(c)** show the inversion grid used. In horizontal plots the locations of vertical sections are shown with thick black lines and vice versa. The areas that were not inverted are marked with grey rectangles.

SED
6, 1–36, 2015

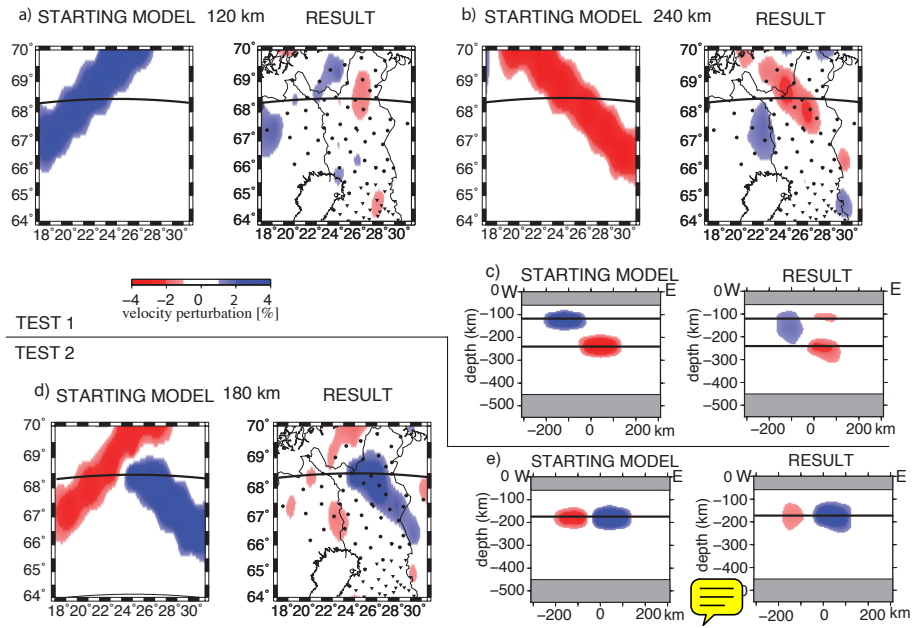

Figure 10. Synthetic test result examples. Two synthetic tests are shown. Test 1 (two horizontal sections in **a, b** and a vertical section in **c**) shows a test with crossing anomalous bodies at the depths of 120 and 250 km. The low velocity anomaly is located beneath Belomorian Mobile Belt, a hypothetical location for an anomaly and the high velocity body above it crosses it perpendicularly. Test 2 (a horizontal and vertical panel in **d** and **e**, respectively) shows another test with anomalies horizontally in same locations but now at the same depth. The locations of vertical sections are shown in horizontal sections with thick black lines and vice versa. The thin lines show the horizontal inversion grid. In horizontal results plots the seismic stations are marked with dots. In vertical sections the cells not inverted are marked with grey rectangles.

SED
6, 1–36, 2015

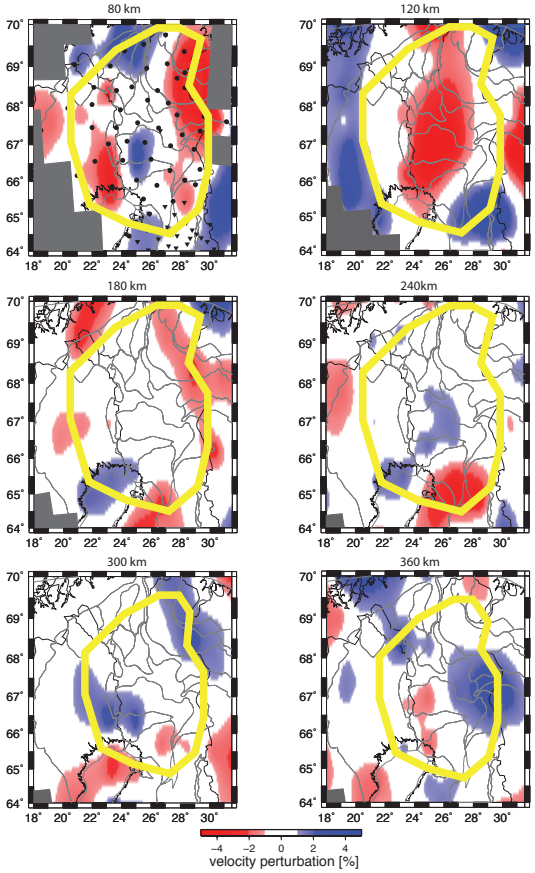

Figure 11. Horizontal sections through our final inversion result. The depth of each section is marked on top of the figure. The grey corners show areas that were crossed by no rays and consecutively were excluded from inversion. The fairly well resolved area of the model is shown for each depth with yellow line.

SED
6, 1–36, 2015

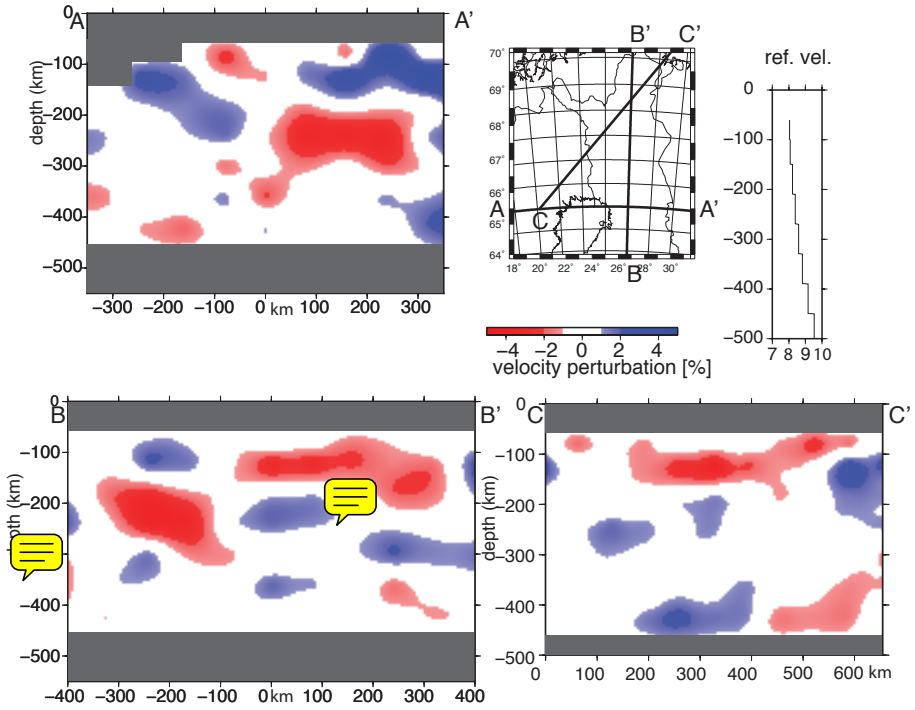

Figure 12. Vertical sections through our final inversion result. The locations of the sections are shown as black lines on the map also showing the horizontal grid. In addition to vertical section we show here the reference velocity curve used (modified from ~~IASP91~~ reference model, Kennett and Engdahl, 1991). The areas where no inversion was done are shown in grey colour.

SED
6, 1–36, 2015

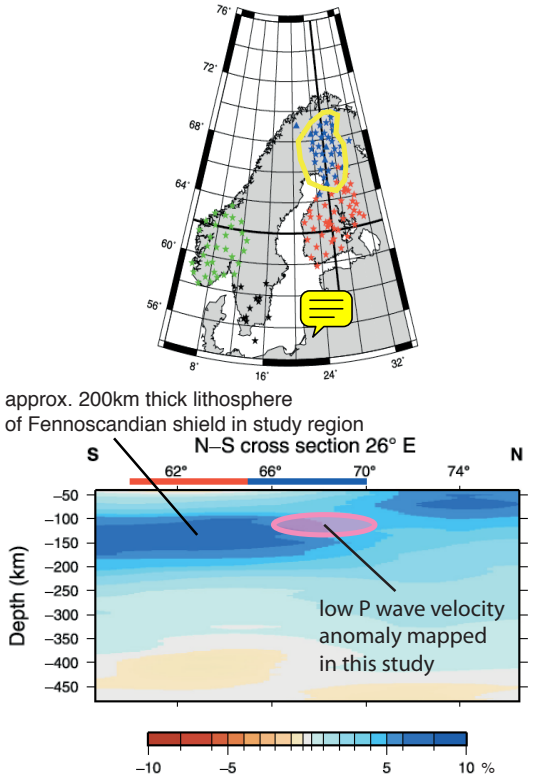

Figure 13. Comparison to previous lithosphere thickness results. The figure has been modified from Pedersen et al. (2013) an it shows the S-wave velocity obtained structure obtained in that study in comparison to global S-wave velocity model by Debayle and Ricard (2012). The area outlined with yellow line shows the well-resolved part of our model at the depth of the low velocity anomaly found in the upper mantle.

SED
6, 1–36, 2015

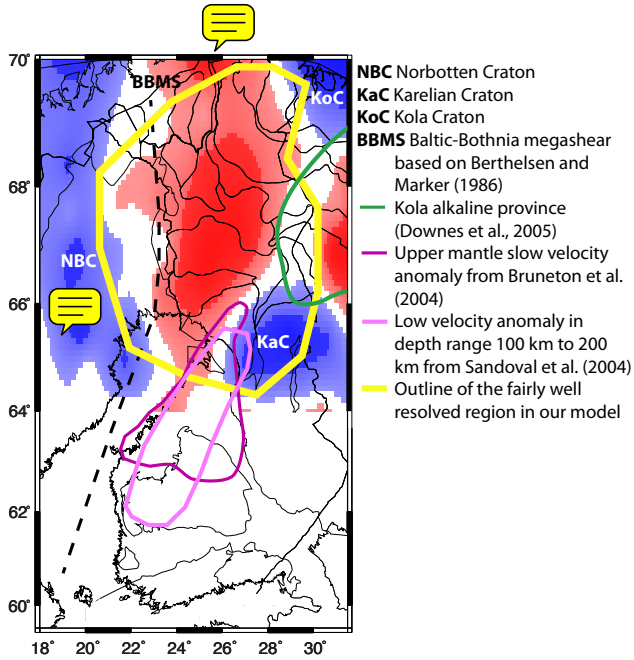

Figure 14. Our results at the depth of 120 km together with cratonic units in our study area and locations of the Kola alkaline province, an upper mantle low velocity anomaly found in SVEKALAPKO data by Bruneton et al. (2004) and Sandoval et al. (2004) and Baltic-Bothnia megashear.

SED
6, 1–36, 2015